Regeneration of degraded Li-rich layered oxide materials through heat treatment-induced transition metal reordering

Yixuan Li [a], Mateusz J. Zuba [c], Shuang Bai [a], Zachary W. Lebens-Higgins [d], Bao Qiu [e], Susie Park [a], Zhaoping Liu [e], Minghao Zhang [a,*], Louis F.J. Piper [c,d,*], Ying Shirley Meng [a,b,*]

[a] Department of NanoEngineering, University of California, San Diego, La Jolla, CA 92093, United States
[b] Materials Science and Engineering, University of California, San Diego, La Jolla, CA 92093, United States
[c] Materials Science & Engineering, Binghamton University, Binghamton, NY 13902, United States
[d] Department of Physics, Applied Physics & Astronomy, Binghamton University, Binghamton, NY 13902, United States
[e] Ningbo Institute of Materials Technology and Engineering (NIMTE), Chinese Academy of Sciences, Ningbo 315201, PR China

ARTICLE INFO

ABSTRACT

Lithium-rich layered oxides (LRLO) have drawn great attention recently as a high energy density cathode material. However, the practical deployment of this materials is hindered by voltage and capacity decay during electrochemical cycling. Applying mild thermal energy to cycled LRLO materials allows to recover the decayed voltage. In this work, a detailed mechanism study of the voltage and structure recovery is conducted through various analytical tools. Heat treatment provides the necessary energy for the transition metal to overcome the kinetic barrier to move from honeycomb center to honeycomb vertex and recover the honeycomb ordering in the transition metal layer. An ambient-air relithiation using Li+ molten salt was also conducted along with the heat treatment to the cycled LRLO cathode and lead to a material regeneration in both the voltage and capacity. This work identifies the transition metal reordering as the key factor under the structure recovery of degraded LRLO materials. It opens a door for the promising strategies to mitigate the voltage and capacity degradation problem in LRLO and provides the potential routes to recycle degraded LRLO materials.

1. Introduction

Rechargeable lithium-ion batteries (LIBs) have been widely studied over the last several decades [1,2]. The recent boost of electric vehicles and scale level energy storage has put even more challenge on the development of LIB cathode materials with high energy density and high power density [3,4]. The study of many conventional LIB cathode materials including $LiCoO_2$ (LCO), $LiFePO_4$ (LFP), and $LiNi_{1/3}Mn_{1/3}Co_{1/3}O_2$ (classical NMC) have been pushed to their theoretical limits, yet those materials cannot provide a specific capacity over 274 mAh/g [5]. LIB cathode materials delivering higher capacity are vital to meet the growing energy density requirements [6]. Among all the candidates, Lithium-rich layered oxides (LRLO) are considered one of the most promising next-generation high energy LIB cathodes due to their large specific capacity (over 300 mAh/g) [7,8]. The LRLO materials are denoted in two ways in the literature: one is a nano-composite structure as $xLi_2MnO_3 \cdot (1-x)LiMO_2$ (M= Ni, Co, Mn or other transition metals (TMs)) proposed by Thackeray et al., [9] another is a single phase solid solution as Li $[Li_xM_{1-x}]O_2$ proposed by Dahn et al. [10]. Both denota-

tion represents the same category of material. In LRLO materials, lithium ions intersperse into both the lithium layer and the TM layer of close packed oxygen framework, typically arranged as an O3 layered structure [11,12]. Within the TM layer, the Li atoms and TM form a honeycomb superstructure where Li sits at the center of each hexagon [10,13]. During charge and discharge, LRLO materials experience the redox of $TM^{3+}/^{4+}$ or $TM^{2+}/^{3+}/^{4+}$ with simultaneous extraction/insertion of Li ions, which is similar to classical NMC layered oxides. However, the cationic redox alone is not sufficient to enable the large capacity observed in LRLO materials. Thus, oxygen activity, or commonly referred to as anionic redox activity, is considered providing a significant portion of the large capacities in LRLO. Many mechanisms have been proposed to explain the anionic redox in layered alkali transition metal oxides, mainly fall into three categories involving peroxo-like species, the formation of oxygen electron holes, or bulk O_2 molecules. Sathiya et al. observed the formation of peroxo-like (O_2^{n-}) species in $Li_2Ru_{0.75}Sn_{0.25}O_3$ and proposed the anionic redox between O^{2-} and O_2^{n-}. [14] McCalla et al. further determined the limits on the value n to be 3.0 - 3.3 for O_2^{n-} species [15]. However, Luo et al. pointed out that the formation of lo-

calized oxygen electron holes is the key to promote the localization, but not the formation, of $O_2{}^{2-}$ peroxide species in $Li_{1.2}Ni_{0.13}Mn_{0.54}Co_{0.13}O_2$ [16]. In the same material, Zhao et al. detected a localized oxygen lattice distortion through neutron PDF and proposed that there is a π-type overlap between the oxidized oxygen ions [17]. More recently, House et al. proposed the formation of molecular O_2 inside the solid as the source of oxygen redox, and those molecules reform O^{2-} in the discharge process [18].

Although LRLO is known for its high capacity, the practical applications of LRLO materials are limited by several drawbacks, such as large irreversible capacity loss (20%−30%) at the initial cycle as well as the continuous capacity and voltage decay in the extended cycling [19,20]. In the applications that require stable voltage such as electric vehicles, the voltage fade in LRLO is especially detrimental [21,22]. The performance limitations of LRLO are usually correlated to the structure degradation and defects generation during cycling [23,24]. The structure degradation has been discussed through many different aspects such as the formation of oxygen vacancies, [20] the migration of TM atoms, [12] the formation of spinel phase, [25] and the accumulation of defects and microstrain [26]. To mitigate the voltage decay problem, many modification methods have been explored in the field. Coating layers such as Al_2O_3 and graphene oxide were introduced to LRLO materials to protect it from the harmful surface-electrolyte reaction and to restrict oxygen evolution and the subsequent TM migration [27,28]. The use of doping elements such as Al, Mg, Mo were also explored by many groups and proved to be able to alter the electronic structure and stabilize the voltage and capacity fade [29,30]. In addition, novel electrolytes with salt additives also show promising results through the improved charge-transfer resistance and cycling stability [31,32].

Different from those modification strategies which mostly works on the pristine material, our group proposed a mild heat treatment method on the cycled material [33]. Our work revealed that the metastable state of cycled LRLO rooted from structural defects is responsible for the voltage decay, and that a structure and voltage recovery can be established by driving the metastable state to stable state with thermal energy. The reappearance of the honeycomb structure and Li migration from Li layer to TM layer was also observed in the heat treated sample. However, the recovery mechanism of the honeycomb structure was not well elaborated in our previous study. In this work, the TM reordering is identified as the key step for the reappearance of the superlattice honeycomb ordering as well as the voltage recovery, and a clear reordering pathway is calculated. This work employs a series of in-situ characterization tools to view the structure evolution under real heating and cooling process and to understand the recovery from the TM environment perspective. In addition, heat treatment itself only recovers the voltage, but not the capacity in cycled LRLO. To solve this problem, an ambient-air relithiation was conducted on cycled LRLO materials to recover the Li loss induced capacity decay. The structure and voltage recovery induced by heat treatment, and the capacity recovery achieved through relithiation, together provide a pathway for the regeneration of the cycled LRLO materials.

The information in this article is discussed in the following major segments: (1) the structure recovery in LRLO is characterized through the increased Li occupancy in TM layer, the reappearance of the superlattice structure, and the improved ordering in the TM environment; (2) a comparison to classical layered oxides without TM superstructure is performed to validate the hypothesis of structure recovery driven by TM reordering; (3) based on the findings in the experimental characterization, a potential TM reordering pathway in cycled LRLO under heat treatment is proposed and proved by first-principles calculations; (4) the heat treatment induced voltage recovery is combined with an ambient-air relithiation process to enable cycled LRLO regeneration.

2. Experimental methods

2.1. Preparation of cycled materials

$Li[Li_{0.144}Ni_{0.136}Co_{0.136}Mn_{0.544}]O_2$ (denoted as LR-NCM) was synthesized through co-precipitation method. The detailed synthesis procedure can be found in our previous publication [34]. $LiNi_{0.8}Mn_{0.1}Co_{0.1}O_2$ (denoted as NMC811) was a commercial sample purchased from Shenzhen Beiterui Battery Materials Co., Ltd. Cycled LR-NCM and NMC811 powders were obtained from pouch cells with graphite anode. The cathode electrode was formed by active material: conductive agents: PVDF with a weight ratio of 94.5:3:2.5. The graphite anode has a mass ratio of graphite: conductive agent: binder = 95:2:3. The LR-NCM cell was cycled between 2.0-4.65 V; the NMC811 cell was cycled between 2.6 V and 4.3 V. The cells were stopped after the initial cycle. After cycling, the full cells were disassembled in an Ar filled glovebox. The cathode electrodes from each cell were washed with DMC to remove the extra $LiPF_6$ salt on the surface, and then the electrode materials were scratched from the electrode and dried in vacuum at room temperature overnight. All materials were stored in the glovebox for further characterizations.

2.2. Regeneration of cycled materials

Cycled LR-NCM materials were hand mixed with an excess amount of a eutectic Li salt mixture in mortar and pestle for 30 minutes. The Li salt mixture contains $LiNO_3$ and $LiOH \cdot H_2O$ with a molar ratio of 3:2. The mixture was heated at 300°C for 15 hours for regeneration, and washed with deionized water to remove the excess amount of Li salts. The regenerated LR-NCM was dried in vacuum oven at 50°C overnight.

2.3. Electrochemistry tests

The pristine material was mixed with polyvinylidene fluoride (PVDF, HSV900, Kynar) and conductive agent (Super C65, TIMCAL) with a ratio of 8:1:1 to prepare the electrode. The cycled material containing 3% conductive agent and 2.5% PVDF was mixed with appropriate amount of Super C65 and PVDF to have a final mass ratio between cycled material: PVDF: Super C65 = 8:1:1. The mix was then well dissolved in a proper amount of N-Methyl-2-pyrrolidone (NMP, $\geq$ 99%, Sigma-Aldrich)) and mixed through the mixer (ARE-310, Thinky Corporation, Japan) in a plastic jar with 4 ZrO_2 beads to form the slurry. The slurry was casted onto Al foil and dried at 80°C in vacuum oven for 12 hours. The electrode was punched into cathode discs with 14 mm diameter with a loading around 4 mg/cm^2. CR2016 coin cells were assembled in the glove box under argon atmosphere, with lithium metal as anode, Celgard 2325 as separator, and 1M LiPF6 in EC:DMC = 3:7 (V:V) as electrolyte (Gotion, USA). LR-NCM cells are cycled between 2.0-4.8 V with C/20 for the initial cycle and C/10 for the rest of the cycles (1C=250 mA/g). NMC811 cells are cycled between 2.5-4.7 V with C/10 for the first two cycles and C/3 for the rest of the cycles (1C=180 mA/g). All cells are rested for 6 h before testing. The electrochemical performances of the assembled coin cells were tested at room temperature either by Neware Battery Test System (Neware Technology Ltd., China) or Arbin BT2000 instruments (Arbin instrument, USA).

2.4. Neutron powder diffraction

High quality neutron powder diffraction (NPD) with *in-situ* heating and cooling were conducted at POWGEN beamline at the Spallation Neutron Sources (SNS) in Oak Ridge National Laboratory (ORNL). 500 mg of the cycled LR-NCM or cycled NMC811 were placed in the beam. Quartz tube was used as the sample container to reduce the background signal. A gas environment containing 80% nitrogen and 20% oxygen was used during the experiment. The SNS was operating at a nominal

of 1100 kW. The center wavelength for the data collection was 1.5 Å. Neutron diffraction data were collected while simultaneously heating the material from 50°C to 400°C and cooling from 400°C to 80°C. At each 25°C interval, a one-hour data collection was performed to acquire diffraction data. The neutron diffraction patterns were characterized using Rietveld refinement with GSAS-II [35] software to extract structural changes.

2.5. Synchrotron X-ray diffraction and pair distribution function

Ex-situ synchrotron XRD (sXRD) and pair distribution function (PDF) data were collected at 11-ID-B in Advanced Photon Source (APS) at Argonne National Laboratory with a wavelength of 0.2115 Å. Around 20 mg of each powder samples were loaded into Kapton capillaries and 5 min total scan time were collected for each sample. GSAS-II was used to extract the XRD pattern as well as performing Rietveld refinement to the collected data. PDF 2D data was calibrated and integrated with GSAS-II. The calibration was done with CeO_2. PDF suite [36] was used to extract PDF patterns and to process G(r) functions. The Q-max used for the Fourier transfer is 20.5 Å^{-2}.

2.6. Transmission electron microscopy

The powder samples were dispersed on TEM lacey carbon grid inside Ar glovebox. The loading and transferring grids to transmission electron microscopy (TEM) were carefully executed to prevent air exposure. TEM was performed on a field emission gun JEOL2800 at 200kV with Gatan OneView Camera (full 4K*4K resolution). Scanning transmission electron microscopy (STEM) and energy dispersive spectroscopy (EDS) was performed on primary particles using a JEOL2800 at 200 kV in ADF mode.

2.7. X-ray absorption near edge structure and extended X-ray absorption fine structure

Temperature-dependent Mn, Ni, & Co K-edge X-ray absorption near edge structure (XANES) and extended X-ray absorption fine structure (EXAFS) measurements were performed on cycled LR-NCM and cycled NMC811 material at beamline 12-BM at APS. The beamline is equipped with a Si (111) double crystal monochromator. Edge measurements were performed concurrently and in steps up to 400°C under normal atmosphere conditions. Edge measured were done in tandem with their reference foils used for energy calibration. A 5-minute rest period for each temperature step was implemented to ensure an equilibrated temperature. ATHENA software from the IFEFFIT package [37,38] was used to carry out the data processing. A model function was generated by performing ab-initio calculations using the code FEFF8.2 [39] and least-squares fit to the data using ARTEMIS software from the IFEFFIT package.

2.8. Computation methodology

The energy states of cycled LR-NCM and heat-treated LR-NCM were performed in the spin polarized GGA+U approximations to the Density Functional Theory (DFT) as implemented in the Vienna ab initio simulation package (VASP) [40]. The same effective U value as applied in our previous report was used to enforce the effect of localized d electrons of the transition-metal ions [30]. We used the PBE exchange correlation, and a plane-wave representation for the wave function with a cutoff energy of 520 eV [41]. The Brillouin zone was sampled with a dense k-points mesh by Gamma packing. The crystal structure of $Li_{14}Ni_3Mn_7O_{24}$ was used as a starting point in the simulation. A specific $Li_{12/14}$ concentration with one oxygen vacancy was chosen to simulate the discharged state obtained experimentally. The full range of different configurations for the unit cell of $Li_{12}Ni_3Mn_7O_{23}$ were tested in our previous work. The lowest energy model with one Li vacancy in Li layer and the other

Li vacancy in TM layer was employed in this work. And then transient state was simulated by moving the neighboring TM to the Li vacant site in TM layer. The nudged elastic band (NEB) method was used to find the minimum-energy path and the energy barrier for lithium and TM migration.

3. Results and discussion

The electrochemistry performance of pristine LR-NCM is shown in Fig. S1(a). In the first cycle, the low initial Coulombic efficiency of 83.8% indicates the structure degradation along with electrochemistry reaction [19,20]. The oxygen plateau disappears after first cycle, leading to a huge drop in the average discharge voltage and the overall energy density. In the following cycles, more decrease in discharge capacity and discharge voltage is observed, indicating continuous structure degradation with cycling [42,43,12]. As shown in Fig. 1(a), heat treatment was conducted on initially cycled LR-NCM with different temperatures, and the voltage recovery is observed in heat treated samples. The four samples with different annealing temperatures all deliver similar amount of discharge capacity since no extra amount of Li was introduced to the samples during heat treatment. The plateau region reappears in the 300°C heat-treated sample. This plateau originates from the Li-O-Li configuration between Li layer and Transition metal (TM) layer [44,45]. The reappearance of the plateau indicates structure recovery of cycled LR-NCM after heat treatment. Similar trend is observed with the LR-NCM after long cycling. Heat treatment was performed to 50-cycled LR-NCM and the electrochemistry performance comparison of heated and unheated samples are shown in Fig. S1(b). The plateau region in the voltage profile reappears in the 300°C heat-treated sample too. All heat-treated samples in the following part of this work are heated at 300°C for 1 hour since it shows the best performance in the electrochemistry testing.

To investigate the origin of this voltage and structure recovery, synchrotron X-ray diffraction (sXRD) and neutron powder diffraction (NPD) were used to characterize the structural changes of cycled LR-NCM over the heat treatment. Fig. 1(b) shows the superlattice peak region of the sXRD pattern of the collected samples. After just the first cycle, the superlattice peak of LR-NCM almost disappears, implying severe degradation of the honeycomb structure. The superlattice peak appears again after heat treatment, representing the structure reordering in TM layer. NPD with in-situ heating and cooling was conducted to the initially cycled LR-NCM to further explore the recovery of structure. Due to the nature of neutron-atomic nuclei interaction and neutron-unpaired electrons interaction, NPD is believed to be more suitable and capable than XRD in probing light elements such as Li [46,47]. Fig. S2(a) shows the collected NPD patterns during the in-situ heating and cooling, and the contour plot of NPD patterns with temperature is shown in Fig. 1(c). No additional peaks were developing during the heat treatment, indicating that the bulk structure maintains well under the heating. It can be clearly seen that most changes happen after 200°C, meaning that there is a threshold of the temperature needed to recover the voltage and structure in the cycled LR-NCM.

Rietveld refinement was performed on the collected NPD patterns to quantify the structure changes of LR-NCM over the heat treatment. Fig. S2(b) shows a representative refined pattern of the initially cycled LR-NCM. The NPD pattern can be well indexed to R-3m space group, with lattice parameter a = 2.859 Å and lattice parameter c = 14.326 Å. The obtained refinement results for the whole in-situ heating and cooling process are plotted in Fig. 1(d). Both lattice parameter a and c show a non-linear increase in the heating and rapid linear decrease in the cooling, indicating that the heating process is a combination of thermal expansion and structure transformation. After heat treatment, both lattice a and c are relaxed to an even lower value than the ones before heating. The irreversible lattice parameter expansion of LR-NCM during cycling is usually assigned to the increased structure disorder coming from the strain accumulation, lithium deficiency, or formation
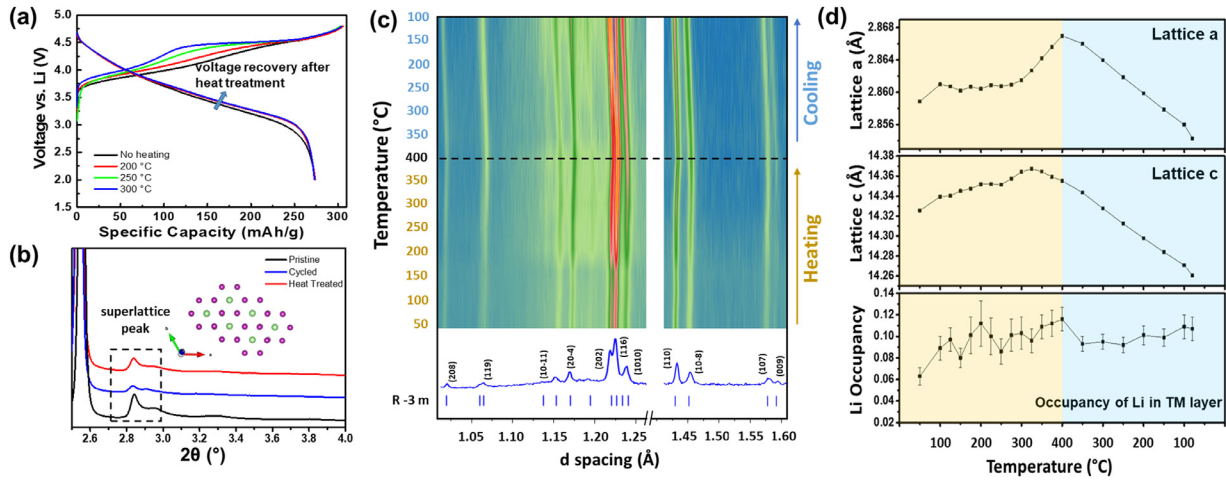
Fig. 1. (a) The 2nd cycle voltage profile of LR-NCM after initial formation cycle before and after heat treatment; (b) Ex-situ sXRD data of pristine LR-NCM, initially cycled LR-NCM, and cycled LR-NCM after heat treatment; (c) Contour plot of the NPD data of cycled LR-NCM with in-situ heating and cooling; (d) Rietveld refinement results of the NPD patterns, giving the *a* and *c* lattice parameters and the Li occupancy in the TM layer.
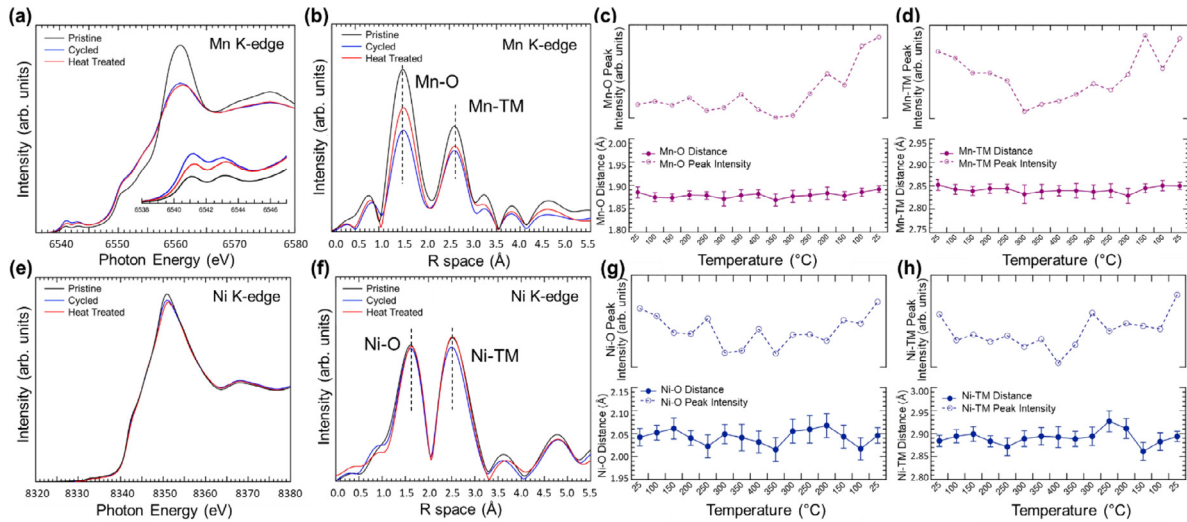

Fig. 2. XAS analysis of initially cycled LR-NCM with in-situ heating and cooling: (a) XANES spectra at Mn K-edge with the magnified pre-edge features; (b) EXAFS spectra at Mn K-edge; (c) Fitting results for Mn-O bond; (d) Fitting results for Mn-TM bond; (e) XANES spectra at Ni K-edge; (f) EXAFS spectra at Ni K-edge; (g) Fitting results for Ni-O bond; (h) Fitting results for Ni-TM bond.

of new phases such as spinel or other layered structures [48,49]. The shrinkage in lattice parameters after heat treatment indicates the structure recovery of the layered LR-NCM. More importantly, a change in the occupancy of Li atoms in the TM layer is observed from the in-situ NPD. With the increase of temperature, the Li amount in the TM layer increases from 0.063 to 0.116 (with the designed value of 0.144). During the cooling process, the occupancy of Li in TM layer decreases slightly but stabilizes around 0.107 at the end of the cooling. The changes in the Li occupancy indicate that during the heating process, Li atoms could go to the TM layer from Li layer. In the meantime, Li vacancies could form in the Li layer, causing a decrease of Li occupancy in Li layer as well as an increase of Li/Ni mixing in the structure after heat treatment (Fig. S2(c)).

To summarize the findings in sXRD and NPD, an increased occupancy of Li in the TM layer is observed after heat treatment, along with the contraction of lattice parameters and the reappearance of the superlattice peak. Those changes mostly happen during the heating process instead of the cooling, showing that temperature is an essential factor enabling the structure recovery. In this structure, the increased amount of Li in the TM layer could re-create the Li excess environment and

thus re-enable the oxygen plateau and oxygen activities in the following cycling. With Li atoms going back to the TM layer, the electrostatic repulsion between TM atoms becomes alleviated, causing the decrease in lattice *a*. Furthermore, the increase of the Li occupancy in the TM layer should be viewed and analyzed with the reappearance of superlattice peak. It is known that such peaks come from the short-range ordering of Li and TM atoms on a $\sqrt{3}a_{hex.} \times \sqrt{3}a_{hex.}$ superlattice within the TM layer. The reappearance of superlattice peak indicates that Li atoms have site preference when they go to the TM layer, which can be characterized by the changes in TM atoms environment.

To further investigate the changes in the TM environment during the heat treatment, in-situ X-ray absorption near edge structure (XANES) and extended X-ray absorption fine structure (EXAFS) were conducted on the initially cycled LR-NCM. Fig. 2(a) shows XANES spectra at Mn K-edge. Compared to pristine state, a slight shift to lower energy is observed in cycled LR-NCM, corresponding to a slight reduction of Mn, which might be a result of some loss of oxygen during the initial cycle. No obvious edge shift is observed during the heat treatment, meaning that heating is not causing any oxidation state changes. The magnified pre-edge features are also shown in Fig. 2(a) as an inset. The pre-edge
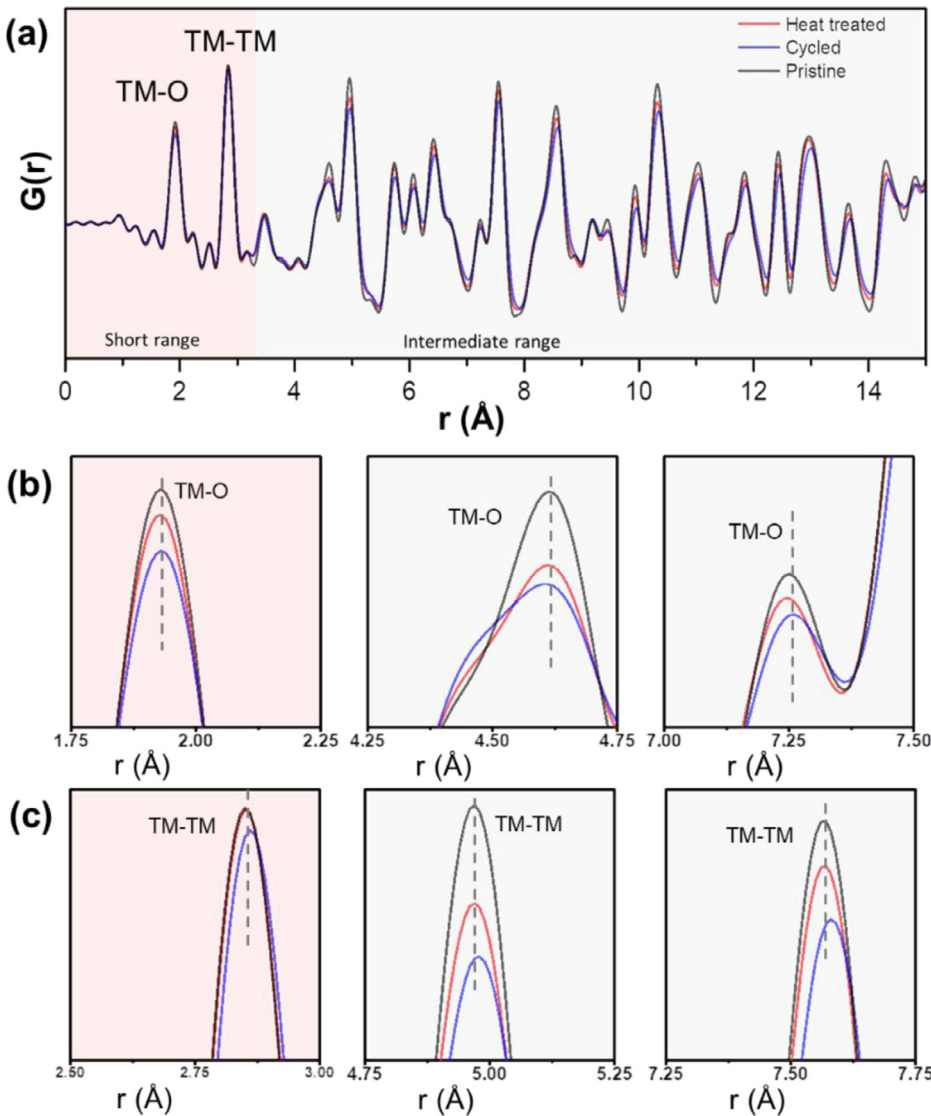
Fig. 3. (a) PDF data of pristine LR-NCM, initially cycled LR-NCM, and cycled LR-NCM after heat treatment; (b) Three magnified regions showing TM-O (re)ordering in pristine sample and after heat treatment; (c) Three magnified regions showing TM-TM (re)ordering in pristine sample and after heat treatment.

region is believed to be very sensitive to the TM-O local structure, where the deviation from centrosymmetry can largely impact the pre-edge environment. The loss of local ordering coming from TM migration and TM-O bond distortion are all proved to contribute to the pre-edge intensity increase in many studies [50,51]. In our case, the Mn K-edge pre-edge intensity significantly decreases in heat-treated sample, which can be attributed to the increased centrosymmetry after heat treatment. The EXAFS spectra at Mn K-edge is shown in Fig. 2(b), where a large increase of the first shell Mn-O intensity and Mn-TM intensity is observed in the cycled LR-NCM after heat treatment, indicating the restoring of superlattice structure as well as the increased ordering in the structure [52,53]. The Mn-TM and Mn-O peak intensity increases should be viewed together with the increased Li amount in the TM layer and the reappearance of the superlattice structure. After first cycling, irreversible Li loss in the TM layer could cause some Li vacancies. The broken honeycomb ordering could also indicate an uneven distribution of positive-charged TM ions in the structure, leading to an overall distortion between TM and O as well as the decrease of Mn-O intensity in EXAFS. After heat treatment, the vacancies in TM layer are filled with Li again and the honeycomb ordering is restored. The restored honeycomb ordering in TM layer leads to an increased Mn-O bond length distribution symmetry in EXAFS, reflected by the increased Mn-TM and Mn-O peak intensity.

Fig. S3 and Table S1 shows the data and corresponding EXAFS fits of LR-NCM before and after heat treatment, with the rest of the data analyzed using the same method. Fig. 2(c-d) shows the fitting results of Mn-O bond and Mn-TM bond obtained from the EXAFS Mn K-edge spectra to quantify the changes of Mn oxidation state and Mn environment ordering during the heat treatment. During the in-situ heating and cooling, no obvious changes can be observed in the Mn-O peak position. The stable peak position validates the conclusion from XANES that Mn remains the same oxidation state during the heat treatment. The Mn-O peak height obtained from the EXAFS fluctuates around its staring point during the heating process, then increases rapidly during the cooling. As discussed above, the peak height depends on the system ordering as well as Debye-Waller factor. As the temperature increases, there is an increase in the Mn environment ordering, which increases the EXAFS signal. However, the Debye-Waller factor also increases with temperature, which decreases the EXAFS signal [54]. The result is competing factors causing the peak height a bit erratic during the heating. After cooling down to room temperature, Mn-O bond shows a clear increase in its intensity. Similarly, an erratic behavior of the Mn-TM peak height is observed at high temperature, and a large increase is observed at the end of the cooling. Intensity increase in both Mn-O bond and Mn-TM bond clearly indicates the reordering of the Mn environment as a result
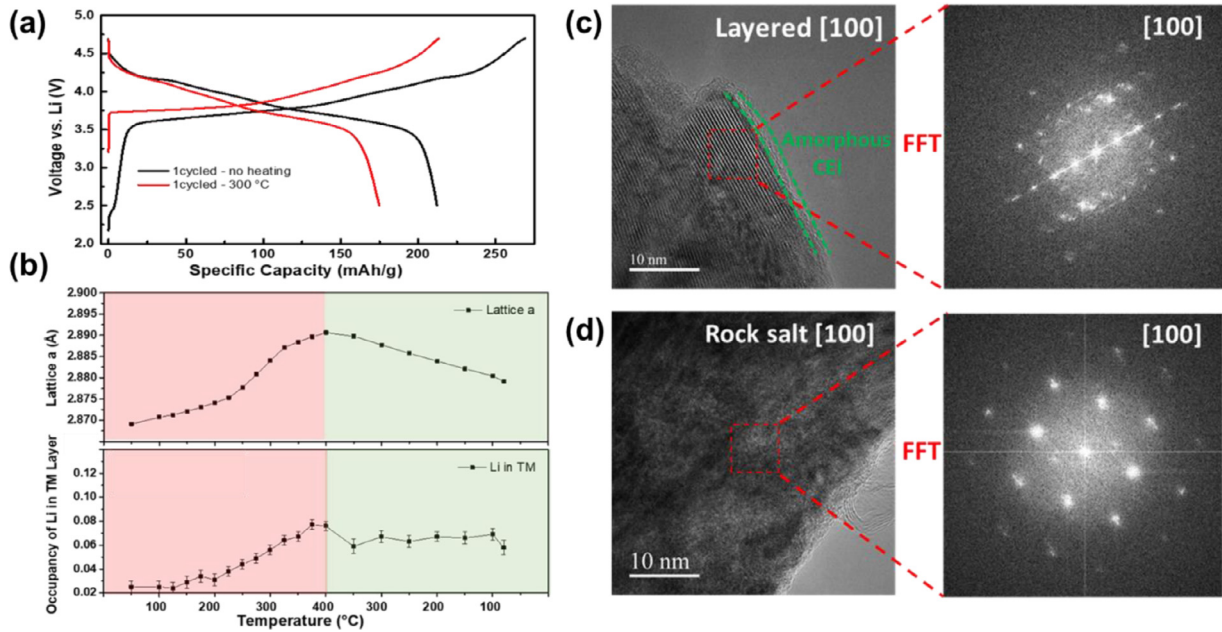
Fig. 4. (a) Voltage profiles of initially cycled NMC811 with and without heat treatment; b) Changes of lattice *a* and Li occupancy in transition metal layer during the heat treatment obtained from Rietveld refinement of the in-situ heating and cooling NPD data; TEM images of NMC811 after initial cycle (c) before and (d) after heat treatment showing layer to rock salt phase transformation.

of the increased Li amount in TM layer and the recovery of the honeycomb structure reordering.

The XANES and EXAFS spectra as well as fitting results at Ni K-edge are shown in Fig. 2(e-h) and Table S2. The XANES spectra shows no oxidation state change in Ni. Similar to the Mn K-edge EXAFS, the Ni-O and Ni-TM intensity also shows an increase after heat treatment, indicating the reordering of Ni environment. The changes of Ni-O and Ni-TM peak position and peak height are quantified through fitting results, where a fluctuation is also observed at high temperature range. The sigma squared value of the TM and O positions obtained through EXAFS fitting are shown in Fig. S4. After heat treatment, the sigma squared value for both Mn K-edge and Ni K-edge is much smaller than cycled state, which also indicates less disordering. The XANES and EXAFS spectra at Co K-edge are shown in Fig. S5. A small edge shift to lower photon energy is observed in the Co XANES spectra, which implies a subtle reduction in Co valence. Co K-edge EXAFS intensity is largely unchanged in the heat treated sample. However, the Co-O peak shift to higher R-space after heat treatment, which agrees with the Co K-edge XANES that there is subtle reduction of Co on the surface. The reduction of surface Co is likely due to an oxygen deficiency in the Co environment, which agrees with the NPD refinement results of oxygen shown in Fig. S2, where a slight decrease of oxygen occupancy is indeed observed after heat treatment.

Confirmed by XANES and EXAFS, TM atoms in the sample is showing an increased ordering in the first shell coordination. Ex-situ Pair Distribution Function (PDF) is conducted on LR-NCM samples to capture the changes of local TM environment in both the short range and the intermediate range. The electron density pair distribution function G(r) was obtained from the synchrotron X-ray total scattering (both Bragg and diffuse) with high real space resolution. The PDF pattern of pristine LR-NCM, initially cycled LR-NCM, and initially cycled LR-NCM after heat treatment are collected and compared in Fig. 3(a). The overall structure of three samples are identical with no additional peaks found in any sample, indicating that TM framework maintains well in the heat treatment. The atom-atom distances are calculated from the LR-NCM structure from NPD refinement and the selected regions are listed in Table S3. Based on the distances of different atom-atom pairs, the PDF patterns are divided into two regions as short range (first coordination

shell) and intermediate range (larger than first coordination shell). In the short range, peaks at a distance shorter than 1.9 Å do not correspond to any atom-atom pairs since those peaks are just termination ripples from the Fourier transform at a finite Q [55]. The first peak around 2 Å is assigned to the TM-O pair, where TM corresponds to the cations in the TM layer. Fig. 3(b) shows the magnified TM-O correlation regions in both the short range and the intermediate range. These regions are chosen because the TM-O pair length has lowest overlap with TM-TM atom pairs within these range. Compared to the pristine state, the intensity of TM-O peaks dropped largely after first cycle, showing an increased displacement. In line with EXAFS result, PDF also shows that the TM-O peak intensity of the cycled LR-NCM increased after heat treatment, indicating an increased ordering of the TM environment. However, the TM-O peak intensity of the heat treated sample is still lower than the pristine state, meaning the partial structure recovery by heat treatment. Fig. 3(c) shows the magnified regions of TM-TM correlations, where an increase of TM-TM peak intensity is observed after heat treatment. The increase of TM-TM intensity is directly related to the reappearance of the superlattice peak, indicating the reordering of Li atoms and TM atoms in the TM layer. PDF results are in good agreement with EXAFS data and the increase in TM-TM and TM-O peaks confirm the increased ordering of TM environment in both short range and intermediate range.

Similar heat treatment experiments were performed to cycled NMC811 as a comparison. NMC811 also employs O3 layered structure like LR-NCM but does not have excess Li in the TM layer to form the TM ordered honeycomb structure. Fig. 4(a) shows the voltage profiles of initially cycled NMC811 before and after heat treatment, with cell configuration details in Table S4. Being the opposite of the LR-NCM case, the heat treated NMC811 exhibits much lower discharge capacity and an increased hysteresis compared to the one without heating. The average discharge voltage for the following cycles in both samples are compared in Fig. S6(a), where the heat treated NMC811 shows continuously lower discharge voltage and faster voltage decay then the non-treated one. In-situ NPD was performed to the initially cycled NMC811 following the same heating and cooling procedure as the cycled LR-NCM, and the Rietveld refinement results are discussed in Fig. 4(b). An increase of lattice parameter *a* can be observed during the heating, and the value of lattice *a* after cooling is still higher than the starting point. An over-
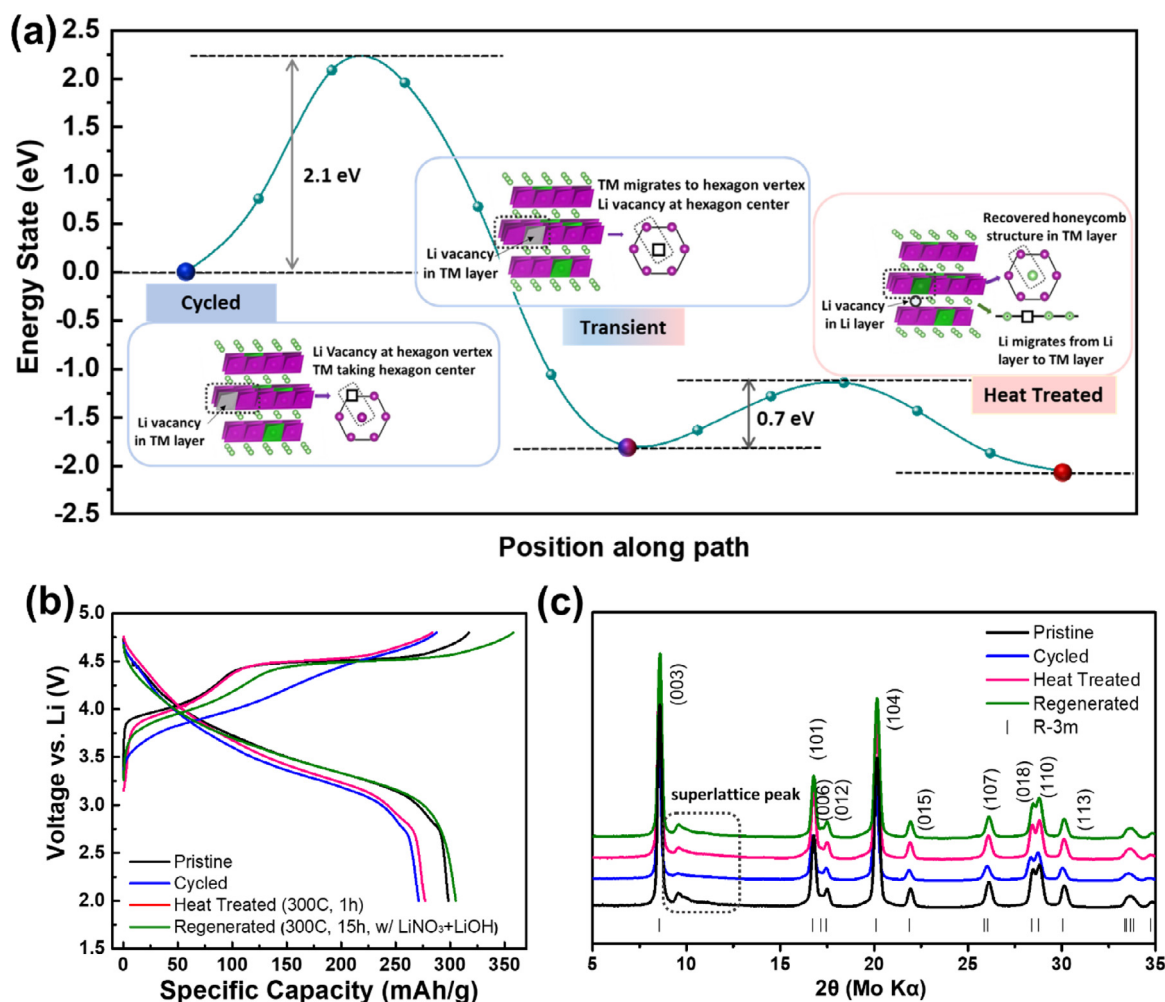
Fig. 5. (a) Schematic energy map of cycled LR-NCM under heat treatment. The energy of three different states (cycled, transient, heat treated) were calculated, the kinetic energy barriers between each state are also shown in the figure. (b) Voltage profiles and (c) XRD patterns of the 1cycled LR-NCM under different regeneration conditions are also compared.

all structure expansion is also seen after heat treatment as suggested by the refinement results in Fig. S7, showing an increased level of disordering induced by heat treatment. Interestingly, the occupancy of Li in the TM layer in the cycled NMC811 also increases from 0.025 to 0.058 during the heat treatment. However, NMC811 does not have any "excess" Li in the TM layer in the pristine structure. The observed huge increase can only be attributed to the increase of Li/Ni mixing in the structure. The increased cation mixing can be correlated with the unwanted phase transformation happening during the heat treatment, as can be seen in the TEM images in Fig. 4(c-d). Despite an amorphous cathode-electrode interface (CEI) layer forming on the surface, the initially cycled NMC811 keeps layered structure after cycling. After heat treatment, the formation of rock salt phase can be clearly identified. More TEM images of the initially cycled NMC811 before and after heat treatment are compared in Fig. S8, also showing similar results of the rock salt phase transformation after heating, which can be attributed to the TM migration. The STEM-EDX mapping and line scan results of the cycled NMC811 before and after heat treatment also shows large difference (Fig. S9). Before heat treatment, the element distribution of Mn, Ni, and Co from the surface to the bulk is largely uniform. However, TM migration leads to less uniform distribution in single particles after heat treatment, where a lower content of Ni is found on the surface region. The XANES spectra at Ni K-edge is shown in Fig. S10(a), where a shift to the lower energy is found on the heat-treated sample. This Ni reduction ties with the TEM results of the rocksalt phase forma-

tion. The EXAFS spectra at Ni K-edge is shown in Fig. S10(b). Compared to the initially cycled NMC811 before heat treatment, a clear decrease of the TM-O peak intensity is observed after heat treatment, indicating an increased disordering in the TM environment. Overall, heat treatment not only fail to improve electrochemistry performance of cycled NMC811, but also induce more severe TM migration and phase transformation. This indicates that the presence of Li in TM layer and the honeycomb ordering is a key factor in the heat treatment induced structure recovery.

As suggested by a series of characterization tools, heat treatment can successfully induce structure and voltage recovery in cycled LR-NCM, with an increased amount of Li back to TM layer and an increased ordering in the TM environment. To further understand the mechanism behind this structure recovery, computation effort was introduced with a proposed TM reordering pathway. Fig. 5(a) presents a schematic energy map of cycled LR-NCM under heat treatment. Three different states (cycled, transient, and heat treated) are shown in this map, and the kinetic energy barriers are calculated between each state. The simplified local structure of each proposed state is also presented in this figure. At the "cycled" state, an irreversible Li loss happens in the TM layer, and some of the TM ions will move from the vertex of the hexagons to the Li vacancy spot at the center of the hexagons, disrupting the ordered superlattice structure. Such migration happens continuously with increased cycle numbers, leading to the disappearance of the superlattice peak after long cycling. After heat treatment, the

occupancy of Li in the TM layer increases and the superlattice ordering reappears. To achieve the "heat treated" state from "cycled' state, a necessary step will be moving the center TM ion in the hexagon back to the vertex, leaving the center site as a vacancy in the TM layer for the Li ions to insert from Li layer, and this state is named as "transient" state.

The calculated "transient" state is 1.8 eV (per calculation supercell) lower than the "cycled state"; the calculated "heat treated" state is also 0.3 eV lower than the "transient" state, which confirms our hypothesis on the three energy states in the structure recovery. Thermodynamically speaking, this TM reordering pathway should be able to happen spontaneously, bringing in a question mark on the necessity of heat treatment. However, it will be a different story if we take kinetic factors into consideration. After calculating the kinetic barrier needed between each step, it can be clearly seen that a huge kinetic barrier around 2.1 eV appears before the "transient" step. Compared to the step from "cycled" to "transient" state, the kinetic energy needed from "transient" to "heat treated" state is relatively low, around 0.7 eV. Heat treatment provides necessary energy for the migrated TM ions to overcome the kinetic barrier to go back to the vertex of each hexagon. Such a high kinetic barrier also partly explains why the cycled LR-NCM only exhibits partial recovery instead of full recovery under short time heat treatment. Longer heating time might help achieve better TM reordering. Besides that, the irreversible Li loss also makes it impossible for the structure to fully return to the initial TM ordering without introducing any extra Li to the TM layer, which also explains why the heat treatment itself can only recover the voltage, but not the capacity in cycled LR-NCM.

To explore the possibility for fully regenerating cycled LR-NCM (recovering both the voltage and the capacity), ambient-air relithiation was conducted on initially cycled LR-NCM together with the heat treatment at 300°C. The relithiation agent is a mix of $LiNO_3$ and $LiOH \cdot H_2O$ with a molar ratio of 3:2, explored in our previous work [56]. The heating time was prolonged to 15 h for TM ions to better overcome the kinetic barrier between "cycled" state and "transient" state. The initially cycled LR-NCM after 1h heat treatment at 300°C is still denoted as "Heat Treated", while the cycled LR-NCM after 15 h heat treatment with relithation agent is denoted as "Regenerated". Fig. 5(b) presents the voltage profile of initially cycled LR-NCM under different heating or regeneration conditions, with cell configuration details in Table S5. ICP-MS results and the electrochemistry performance of those samples are listed in Table S6. In the heat treated sample, the Li/TM ratio is similar to the cycled LR-NCM. However, a large increase of Li/TM ratio is seen in the regenerated sample, representing the successful relithiation. In Fig. 6(b), the red line represents the heat treated sample, while the green line represents the regenerated sample. Compared to the cycled state, both heated samples show the oxygen plateau in the charge curve again. The average discharge voltage also increases from 3.49 V in the cycled LR-NCM to 3.52 V in the regenerated sample. The voltage and structural recovery from heat treatment is not affected by the presence of relithiation salt. The heat treated sample without relithiation delivers similar capacity (~272 mAh/g) as the cycled sample before heat treatment. But the regenerated sample delivers 305 mAh/g discharge capacity, showing very similar discharge curve as the pristine material represented by the black line. Fig. 5(c) compares the XRD pattern of cycled LR-NCM under different heating or regeneration conditions, where no impurity peaks are found. It also clearly shows that the superlattice peak grows even higher in the regenerated sample compared to the heat treated sample, as a result of the prolonged heating time. Overall, the computation results match well with the proposed TM reordering pathway, showing that heat treatment can successfully recover the TM ordered structure by overcoming the kinetic barrier of moving TM ions back to hexagon arrangement and forming Li vacancies in the TM layer for Li atoms to insert from Li layer. Guided by the calculated TM recovery pathway, prolonged heating time with relithiation was performed to cycled LR-NCM and full regeneration of cycled LR-NCM was achieved.

4. Conclusions

Cycled LR-NCM materials show voltage and structure recovery after heat treatment. In this work, the mechanism of the voltage and structure recovery was investigated from the perspective of TM reordering. sXRD and NPD experiments proved Li migration from Li layer to TM layer, recreating the local Li-excess environment, accompanied by the reappearance of superlattice ordering and the contraction of overall lattice. EXAFS and PDF confirmed the increased ordering of TM environment in both the short range and the intermediate range. A TM reordering pathway was proposed and evaluated with computation methodology, where a kinetic barrier to move TM ions to reform the honeycomb frame is believed to be the controlling step in this heat induced structure and voltage recovery. To validate the hypothesis, heat treatment was repeated in cycled NMC811 which shares a very similar layered structure as LR-NCM but lacks TM ordering in the pristine state. The heat treatment could only induce TM migration and lead to rock-salt phase transformation in this case, which again proves the importance of TM ordering. Guided by the computation effort, regeneration of cycled LR-NCM was achieved through heat treatment and ambient-air relithiation at one step, recovering both the voltage and the capacity. The findings in this study shed light on the possibility of utilizing other energy forms such as pressure or photon to induce structure and voltage recovery in cycled Li-rich materials. The underestimated role of TM ordering also directs the rational design of future LRLO materials where a stable TM ordering environment is preferred.

Author contribution

Y.L., M.Z., and Y.S.M. designed the experiments. Y.L. conducted the in-situ NPD measurements and refinement. M.J.Z. and Z.W.L. conducted the in-situ heating XANES and EXAFS experiments. M.J.Z. did the EXAFS fitting analysis. Y.L. conducted the ex-situ sXRD and PDF measurement and analysis. S.B. and M.Z. conducted TEM and STEM-EELS experiments and analysis. M.Z. performed the computation work. B.Q. and Z.L. provided the cycled LR-NCM and NCM811 materials. Y.L., B.Q. and S.P. conducted electrochemistry testing. Y.S.M., M.Z., and L.P. supervised the research. Y.L wrote the manuscript. All authors contributed to the discussion and provided feedback on the manuscript.

Declaration of Competing Interest

The authors declare no conflicts of interest.

Acknowledgments

Supplementary materials

Supplementary material associated with this article can be found, in the online version, at doi:10.1016/j.ensm.2020.11.013.

References

[1] Y. Li, Y. Bai, X. Bi, J. Qian, L. Ma, J. Tian, C. Wu, F. Wu, J. Lu, K. Amine, ChemSusChem 9 (2016) 728.

[2] T. Kim, W. Song, D.Y. Son, L.K. Ono, Y. Qi, J. Mater. Chem. A 7 (2019) 2942.

[3] B. Xu, D. Qian, Z. Wang, Y.S. Meng, Mater. Sci. Eng. R Rep. 73 (2012) 51.

[4] B. Lee, Z. Wu, V. Petrova, X. Xing, H. Lim, H. Liu, J. Electrochem. Soc. 165 (2018) 525.

[5] J. Ye, Y.X. Li, L. Zhang, X.P. Zhang, M. Han, P. He, H.S. Zhou, ACS Appl. Mater. Interfaces 8 (2016) 208.

[6] J.B. Goodenough, Y. Kim, Chem. Mater. 22 (2010) 587.

[7] D. Mohanty, J. Li, D.P. Abraham, A. Huq, E.A. Payzant, D.L. Wood, C. Daniel, Chem. Mater. 26 (2014) 6272.

[8] S. Hy, H. Liu, M. Zhang, D. Qian, B.-J. Hwang, Y.S. Meng, Energy Environ. Sci. 9 (2016) 1931.

[9] J. Hong, H.D. Lim, M. Lee, S.W. Kim, H. Kim, S.T. Oh, G.C. Chung, K. Kang, Chem. Mater. 24 (2012) 2692.

[10] Z. Lu, L.Y. Beaulieu, R.A. Donaberger, C.L. Thomas, J.R. Dahn, J. Electrochem. Soc. 149 (2002) A778.

[11] M.D. Radin, S. Hy, M. Sina, C. Fang, H. Liu, J. Vinckeviciute, M. Zhang, M.S. Whittingham, Y.S. Meng, A. Van der Ven, Adv. Energy Mater. 1602888 (2017) 1.

[12] D. Qian, B. Xu, M. Chi, Y.S. Meng, Phys. Chem. Chem. Phys. 16 (2014) 14665.

[13] Z. Lu, J.R. Dahn, J. Electrochem. Soc. 149 (2002) A815–A822.

[14] M. Sathiya, J.-B. Leriche, E. Salager, D. Gourier, J.-M. Tarascon, H. Vezin, Nat. Commun. 6 (2015) 6276.

[15] E. McCalla, A.M. Abakumov, M. Saubanere, D. Foix, E.J. Berg, G. Rousse, M.-L. Doublet, D. Gonbeau, P. Novak, G. Van Tendeloo, R. Dominko, J.-M. Tarascon, Science 350 (2015) 1516.

[16] K. Luo, M.R. Roberts, R. Hao, N. Guerrini, D.M. Pickup, Y.S. Liu, K. Edström, J. Guo, A.V. Chadwick, L.C. Duda, P.G. Bruce, Nat. Chem. 8 (2016) 684.

[17] E. Zhao, M. Zhang, X. Wang, E. Hu, J. Liu, X. Yu, M. Olguin, T.A. Wynn, Y.S. Meng, K. Page, F. Wang, H. Li, X.Q. Yang, X. Huang, L. Chen, Energy Storage Mater. 24 (2020) 384.

[18] R.A. House, U. Maitra, M.A. Pérez-Osorio, J.G. Lozano, L. Jin, J.W. Somerville, L.C. Duda, A. Nag, A. Walters, K.J. Zhou, M.R. Roberts, P.G. Bruce, Nature 577 (2020) 502.

[19] A. Singer, S. Hy, M. Zhang, D. Cela, C. Fang, B. Qiu, Y. Xia, Z. Liu, A. Ulvestad, N. Hua, J. Wingert, H. Liu, M. Sprung, A.V. Zozulya, E. Maxey, R. Harder, Y.S. Meng, O.G. Shpyrko, Nat. Energy 3 (8) (2017) 641.

[20] C.R. Fell, D. Qian, K.J. Carroll, M. Chi, J.L. Jones, Y.S. Meng, Chem. Mater. 25 (2013) 1621.

[21] E.M. Erickson, F. Schipper, T.R. Penki, J.-Y. Shin, C. Erk, F.-F. Chesneau, B. Markovsky, D. Aurbach, J. Electrochem. Soc. 164 (2017) A6341.

[22] J.R. Croy, M. Balasubramanian, K.G. Gallagher, A.K. Burrell, Acc. Chem. Res. 48 (2015) 2813.

[23] K.A. Jarvis, Z. Deng, L.F. Allard, A. Manthiram, P.J. Ferreira, Chem. Mater. 23 (2011) 3614.

[24] Y.S. Meng, G. Ceder, C.P. Grey, W.S. Yoon, M. Jiang, J. Bréger, Y. Shao-Horn, Chem. Mater. 17 (2005) 2386.

[25] B. Xu, C.R. Fell, M. Chi, Y.S. Meng, Energy Environ. Sci. 4 (2011) 2223.

[26] C.R. Fell, M. Chi, Y.S. Meng, J.L. Jones, Solid State Ionics 207 (2012) 44.

[27] X. Zhang, I. Belharouak, L. Li, Y. Lei, J.W. Elam, A. Nie, X. Chen, R.S. Yassar, R.L. Axelbaum, Adv. Energy Mater. 3 (2013) 1299.

[28] P. Oh, M. Ko, S. Myeong, Y. Kim, J. Cho, Adv. Energy Mater. (2014) 4.

[29] M. Lengyel, K.Y. Shen, D.M. Lanigan, J.M. Martin, X. Zhang, R.L. Axelbaum, J. Mater. Chem. A 4 (2016) 3538.

[30] T.A. Wynn, C. Fang, M. Zhang, H. Liu, D.M. Davies, X. Wang, D. Lau, J.Z. Lee, B.Y. Huang, K.Z. Fung, C.T. Ni, Y.S. Meng, J. Mater. Chem. A 6 (2018) 24651.

[31] P.K. Nayak, J. Grinblat, M. Levi, D. Aurbach, J. Electrochem. Soc. 162 (2015) A596.

[32] Q. Wu, W. Lu, M. Miranda, T.K. Honaker-Schroeder, K.Y. Lakhsassi, D. Dees, Electrochem. Commun. 24 (2012) 78.

[33] B. Qiu, M. Zhang, S.-Y. Lee, H. Liu, T.A. Wynn, L. Wu, Y. Zhu, W. Wen, C.M. Brown, D. Zhou, Z. Liu, Y.S. Meng, Cell Rep. Phys. Sci. 1 (2020) 100028.

[34] B. Qiu, M. Zhang, L. Wu, J. Wang, Y. Xia, D. Qian, H. Liu, S. Hy, Y. Chen, K. An, Y. Zhu, Z. Liu, Y.S. Meng, Nat. Commun. 7 (2016) 12108.

[35] B.H. Toby, R.B. Von Dreele, J. Appl. Crystallogr. (2013) 544 46.2.

[36] C.L. Farrow, P. Juhas, J.W. Liu, D. Bryndin, E.S. Boin, J. Bloch, T. Proffen, S.J.L. Billinge, J. Phys. Condens. Matter (2007) 335219 19.33.

[37] M. Newville, J. Synchrotron Radiat. 8 (2001) 322.

[38] B. Ravel, M. Newville, J. Synchrotron Radiat. 12 (2005) 537–541.

[39] A. Ankudinov, B. Ravel, Phys. Rev. B–Condens. Matter Mater. Phys. 58 (1998) 7565.

[40] D. Joubert, Phys. Rev. B–Condens. Matter Mater. Phys. 59 (1999) 1758.

[41] J.P. Perdew, K. Burke, M. Ernzerhof, Phys. Rev. Lett. 77 (1996) 3865.

[42] M. Ko, P. Oh, S. Chae, W. Cho, J. Cho, Small (2015) 11.33.

[43] B. Qiu, M. Zhang, Y. Xia, Z. Liu, Y.S. Meng, Chem. Mater. 29 (2017) 908.

[44] D.-H. Seo, J. Lee, A. Urban, R. Malik, S. Kang, G. Ceder, Nat. Chem. 8 (2016) 692.

[45] G. Assat, J.M. Tarascon, Nat. Energy 3 (2018) 373.

[46] H. Liu, Y. Chen, S. Hy, K. An, S. Venkatachalam, D. Qian, M. Zhang, Y.S. Meng, Adv. Energy Mater. 6 (2016) 1.

[47] O. Dolotko, A. Senyshyn, M.J. Mühlbauer, K. Nikolowski, H. Ehrenberg, J. Power Sources 225 (2014) 197.

[48] D. Mohanty, S. Kalnaus, R.A. Meisner, K.J. Rhodes, J. Li, E.A. Payzant, D.L. Wood, C. Daniel, J. Power Sources 229 (2013) 239.

[49] B. Song, Z. Liu, M.O. Lai, L. Lu, Phys. Chem. Chem. Phys. 14 (2012) 12875.

[50] H. Koga, L. Croguennec, M. Ménétrier, P. Mannessiez, F. Weill, C. Delmas, S. Belin, J. Phys. Chem. C 118 (2014) 5700.

[51] J. Rana, R. Kloepsch, J. Li, T. Scherb, G. Schumacher, M. Winter, J. Banhart, J. Mater. Chem. A 2 (2014) 9099.

[52] J.R. Croy, K.G. Gallagher, M. Balasubramanian, B.R. Long, M.M. Thackeray, J. Electrochem. Soc. 161 (2013) A318.

[53] X. Yu, Y. Lyu, L. Gu, H. Wu, S.M. Bak, Y. Zhou, K. Amine, S.N. Ehrlich, H. Li, K.W. Nam, X.Q. Yang, Adv. Energy Mater. 4 (2014) 1300950.

[54] G. Dalba, P. Fornasini, J. Synchrotron Radiat. 4 (1997) 243.

[55] D. Zeng, J. Cabana, J. Bréger, W. Yoon, C.P. Grey, Chem. Mater. 19 (2007) 6277.

[56] Y. Shi, M. Zhang, Y.S. Meng, Z. Chen, Adv. Energy Mater. (2019) 9.